The Astrophysical Journal, 842:122 (9pp), 2017 June 20 https://doi.org/10.3847/1538-4357/aa74e0
© 2017. The American Astronomical Society. All rights reserved.
OPEN ACCESS

Nature of Kinetic Scale Turbulence in the Earth's Magnetosheath

C. H. K. Chen[1] and S. Boldyrev[2,3]
[1] Department of Physics, Imperial College London, London SW7 2AZ, UK; christopher.chen@imperial.ac.uk
[2] Department of Physics, University of Wisconsin–Madison, Madison, WI 53706, USA
[3] Space Science Institute, Boulder, CO 80301, USA
Received 2017 March 17; revised 2017 May 3; accepted 2017 May 22; published 2017 June 22

Abstract

We present a combined observational and theoretical analysis to investigate the nature of plasma turbulence at kinetic scales in the Earth's magnetosheath. In the first decade of the kinetic range, just below the ion gyroscale, the turbulence was found to be similar to that in the upstream solar wind: predominantly anisotropic, low-frequency and kinetic Alfvén in nature. A key difference, however, is that the magnetosheath ions are typically much hotter than the electrons, $T_i \gg T_e$, which, together with $\beta_i \sim 1$, leads to a change in behavior in the second decade, close to electron scales. The turbulence here is characterized by an increased magnetic compressibility, following a mode we term the *inertial kinetic Alfvén wave*, and a steeper spectrum of magnetic fluctuations, consistent with the prediction $E_B(k_\perp) \propto k_\perp^{-11/3}$ that we obtain from a set of nonlinear equations. This regime of plasma turbulence may also be relevant for other astrophysical environments with $T_i \gg T_e$, such as the solar corona, hot accretion flows, and regions downstream of collisionless shocks.

Key words: magnetic fields – plasmas – solar wind – turbulence – waves

1. Introduction

Plasma turbulence is widespread, occurring in a variety of astrophysical environments, such as galaxy clusters, the interstellar medium, and stellar winds. It can be modeled as a cascade of energy from large scales, where the energy is injected, to small, kinetic scales (comparable to the ion and electron gyroscales), where it is thought to be dissipated. However, many aspects of how the cascade operates (in particular at kinetic scales), remain to be understood.

The majority of observations of turbulence at kinetic scales are from the solar wind upstream of the Earth's bow shock (e.g., Alexandrova et al. 2013; Bruno & Carbone 2013; Goldstein et al. 2015; Chen 2016). At scales smaller than the ion gyroscale, the energy spectrum of solar wind density and magnetic fluctuations is observed to be a power law in wavenumber, close to $k^{-2.8}$, down to electron scales (e.g., Alexandrova et al. 2009; Kiyani et al. 2009; Chen et al. 2010a, 2012; Sahraoui et al. 2013). Between the ion and electron scales, the fluctuations are anisotropic, with stronger gradients perpendicular to the mean magnetic field rather than parallel, $k_\perp \gg k_\parallel$ (Chen et al. 2010a), and the amplitude of the density fluctuations relative to the magnetic fluctuations indicates that the turbulence is predominantly low frequency, with a polarization consistent with that of the kinetic Alfvén wave (Boldyrev et al. 2013; Chen et al. 2013b). These features can be interpreted as a cascade of kinetic Alfvén turbulence from ion to electron scales (Howes et al. 2008; Schekochihin et al. 2009; Chen et al. 2010b; Boldyrev & Perez 2012).

When the critical balance principle (Goldreich & Sridhar 1995) is assumed, in which the linear and nonlinear terms of the dynamical equations are comparable, dimensional arguments lead to a perpendicular energy spectrum $E(k_\perp) \propto k_\perp^{-7/3}$, along with an anisotropy $k_\parallel \propto k_\perp^{1/3}$ (Cho & Lazarian 2004; Schekochihin et al. 2009). If the cascade is also assumed to accumulate into intermittent 2D structures, these scalings become $E(k_\perp) \propto k_\perp^{-8/3}$ and $k_\parallel \propto k_\perp^{2/3}$ (Boldyrev & Perez 2012). The critical balance principle suggests that the linear physics is relevant, even in a strongly turbulent, intermittent cascade. This is borne out in the solar wind, with a variety of observations showing that the fluctuations follow linear relationships to order unity (e.g., Bale et al. 2005; Sahraoui et al. 2009; Howes & Quataert 2010; He et al. 2011; Podesta & Gary 2011; Yao et al. 2011a; Howes et al. 2012; Klein et al. 2012; TenBarge et al. 2012; Chen et al. 2013b, 2013c; Kiyani et al. 2013; Bruno & Telloni 2015; Telloni et al. 2015; Verscharen et al. 2017), and similarly in numerical simulations (e.g., Howes et al. 2011; Boldyrev & Perez 2012; TenBarge & Howes 2012; Verscharen et al. 2012; Franci et al. 2015; Told et al. 2015; Cerri et al. 2016), although there can also be quantitative differences introduced by the nonlinearites (e.g., Boldyrev et al. 2011, 2012; Chen et al. 2013a, 2013b).

The Earth's magnetosheath, the region of solar wind downstream of the bow shock, presents a different environment in which kinetic scale turbulence can be measured, although it has been less comprehensively studied here. This is partly because there are often additional processes taking place which complicate the picture, e.g., instability-generated waves (such as mirror modes, ion cyclotron waves, and whistler waves) and various other non-turbulent structures (see, e.g., Lucek et al. 2005, for a review). However, with careful data selection, these can be avoided, allowing the pure turbulent cascade to be investigated. It has been shown that at ion scales, the magnetic field spectrum in the magnetosheath steepens (e.g., Dudok de Wit & Krasnosel'skikh 1996; Czaykowska et al. 2001; Alexandrova et al. 2008; Chaston et al. 2008; Yordanova et al. 2008; Yao et al. 2011b; Huang et al. 2014; Stawarz et al. 2016; Matteini et al. 2017), the electric field spectrum flattens (Chaston et al. 2008; Stawarz et al. 2016; Matteini et al. 2017), and the turbulence in the kinetic range is intermittent (Dudok de Wit & Krasnosel'skikh 1996; Sundkvist et al. 2007; Stawarz et al. 2016; Vörös et al. 2016) and anisotropic, with $k_\perp \gg k_\parallel$ (Mangeney et al. 2006; Alexandrova et al. 2008; Stawarz et al. 2016). These features are similar to the upstream

Original content from this work may be used under the terms of the Creative Commons Attribution 3.0 licence. Any further distribution of this work must maintain attribution to the author(s) and the title of the work, journal citation and DOI.

solar wind, which might suggest that a similar type of turbulence is present.

An important difference between the magnetosheath and the upstream solar wind, however, is the ratio of ion and electron temperatures. In the upstream solar wind, the temperatures are typically comparable, $T_i \sim T_e$, whereas in the magnetosheath, the ions are typically much hotter, $T_i \gg T_e$ (Wang et al. 2012), as a result of processing by the bow shock (e.g., Burgess & Scholer 2013; Krasnoselskikh et al. 2013; Vink et al. 2015). We have found that this can lead to a change in the behavior of the turbulence near electron scales. In this paper, we present the identification of this turbulence regime in measurements from the *Magnetospheric Multiscale* (*MMS*) spacecraft, together with a theoretical framework through which it can be understood.

2. Observations

2.1. Data Interval

The observational analysis is based on data from the four *MMS* spacecraft (Burch et al. 2016) during a period in the Earth's magnetosheath (2015 October 16, 09:24:11–09:25:24) for which burst mode data are available. During this time, the spacecraft were located 11.9 R_E from Earth, close to the dusk side magnetopause, with an inter-spacecraft separation of ~14 km. This period does not contain large-amplitude variations in the magnetic field magnitude (associated with mirror modes) or high-frequency wave packets at electron scales (thought to be whistler waves), allowing the pure turbulent cascade to be studied.

For the magnetic field $\boldsymbol{B}$, data from the FGM (Fluxgate Magnetometer, Russell et al. 2016) and SCM (Search-Coil Magnetometer, Le Contel et al. 2016) instruments were combined using a wavelet technique (Chen et al. 2010a) to produce 8192 samples s^{-1} data containing the full range of frequencies (with the crossover between instruments at ~8 Hz). The electric field $\boldsymbol{E}$ was measured by the SDP (Spin-Plane Double Probe, Lindqvist et al. 2016) and ADP (Axial Double Probe, Ergun et al. 2016) instruments at the same resolution. FPI (Fast Plasma Investigation, Pollock et al. 2016) was used for the ion and electron densities n_i and n_e, velocities $\boldsymbol{v}_i$ and $\boldsymbol{v}_e$, and temperatures T_i and T_e; the resolution of these moments is 150 ms for the ions and 30 ms for the electrons. A time series of the data from *MMS3* for this interval is shown in Figure 1. The average plasma conditions were: $B \approx 39$ nT, $n_i \approx n_e \approx 14\,\mathrm{cm}^{-3}$, $v_i \approx v_e \approx 180\,\mathrm{km\,s}^{-1}$, $T_i \approx 210$ eV, $T_e \approx 23$ eV, with temperature anisotropies $(T_\perp/T_\parallel)_i \approx 1.6$ and $(T_\perp/T_\parallel)_e \approx 1.0$. These parameters result in average ion and electron plasma betas $\beta_i \approx 0.79$ and $\beta_e \approx 0.087$ (where $\beta_s = 2\mu_0 n_s k_B T_s/B^2$).

From the magnitude of the ion and electron betas, $\beta_e \ll \beta_i \sim 1$, it can be seen that for the ions, the gyroradius $\rho_i = v_{th\perp i}/\Omega_i$ (where $v_{th\perp i} = \sqrt{2k_B T_{\perp i}/m_i}$ is the thermal speed, $\Omega_i = q_i B/m_i$ is the gyrofrequency, m_i is the mass, and q_i is the charge) and inertial length $d_i = v_A/\Omega_i$ (where $v_A = B/\sqrt{\mu_0 \rho}$ is the Alfvén speed and ρ is the mass density) are similar $\rho_i \sim d_i$, whereas for the electrons, the gyroradius is much smaller, $\rho_e \ll d_e$. This results in two sub-ranges between the ion and electron gyroscales: one above the electron inertial scale, $1/\rho_i < k < 1/d_e$, and one below, $1/d_e < k < 1/\rho_e$. The following sections describe the nature of the fluctuations in each of these ranges.

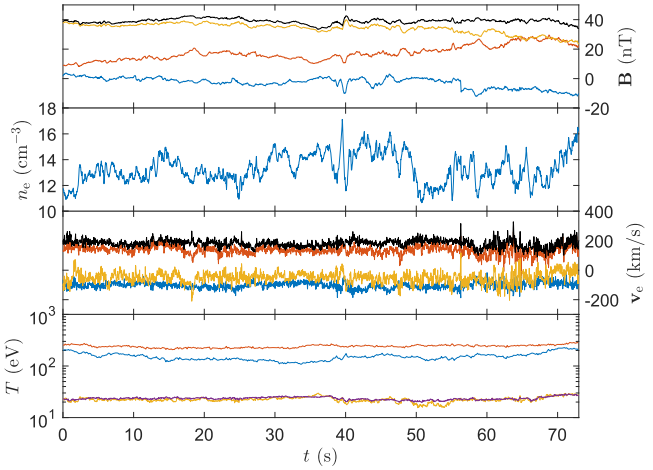


Figure 1. Time series of the magnetic field ($\boldsymbol{B}$) components in geocentric solar ecliptic (GSE) coordinates (blue, orange, yellow) and magnitude (black), electron number density (n_e), electron velocity ($\boldsymbol{v}_e$) components in GSE (blue, orange, yellow) and magnitude (black), and temperatures $T_{\parallel i}$ (blue), $T_{\perp i}$ (orange), $T_{\parallel e}$ (yellow) and $T_{\perp e}$ (purple) from *MMS3*.

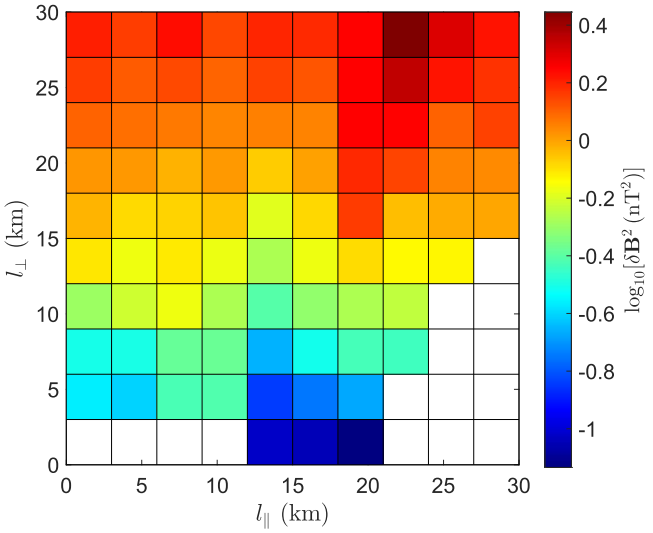


Figure 2. Magnetic fluctuation energy $\delta\boldsymbol{B}^2$ as a function of length scale parallel $l_\parallel$ and perpendicular $l_\perp$ to the local mean field. Contours are elongated in the $l_\parallel$ direction, indicating anisotropic fluctuations $k_\perp \gg k_\parallel$.

2.2. Nature of Fluctuations at $kd_e < 1$

To determine the nature of the fluctuations, first the anisotropy was measured, using the multi-spacecraft technique described by Chen et al. (2010a). Two-point structure functions $\delta\boldsymbol{B}^2(\boldsymbol{l}) = \langle|\boldsymbol{B}(\boldsymbol{x}+\boldsymbol{l}) - \boldsymbol{B}(\boldsymbol{x})|^2\rangle_{\boldsymbol{x}}$ were calculated from the time-lagged magnetic field measurements between pairs of spacecraft. The technique mixes spatial and temporal measurements, and assumes the Taylor hypothesis (Taylor 1938) to be satisfied (i.e., that the measured temporal variations correspond to spatial variations in the plasma frame), which appears to be the case, despite the low flow speed and dispersive regime (see Section 2.4). Figure 2 shows $\delta\boldsymbol{B}^2(\boldsymbol{l})$, binned and averaged as a function of length scale parallel and perpendicular to the local mean field. The range of scales covered is $11 < k\rho_i < 57$, or equivalently $0.29 < kd_e < 1.5$. It can be seen that the contours of $\delta\boldsymbol{B}^2$ are elongated in the parallel direction, and that the value of $\delta\boldsymbol{B}^2$ at a scale of 15 km is ~10 times larger in the perpendicular direction than in the parallel direction. This

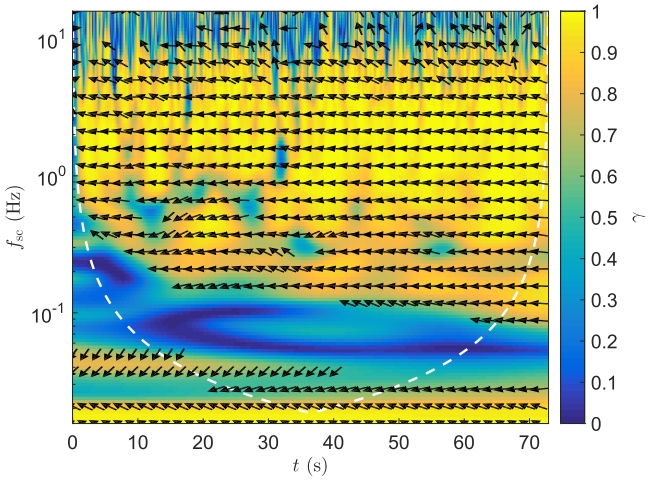


Figure 3. Wavelet magnitude-squared coherence γ and phase ϕ (angle of black arrows from the $+x$ direction) between δn_e and $\delta B_\parallel$. The white dashed line marks the cone of influence. Strong anti-correlation can be seen at spacecraft-frame frequencies 0.5 Hz $\lesssim f_{sc} \lesssim$ 5 Hz.

indicates strongly anisotropic fluctuations $k_\perp \gg k_\parallel$, consistent with previous findings for magnetosheath (Mangeney et al. 2006; Alexandrova et al. 2008) and solar wind (Chen et al. 2010a) turbulence in the kinetic range.

The two possible modes in this regime for an isotropic Maxwellian plasma are the kinetic Alfvén wave,

$$\omega^2 = \frac{k_\parallel^2 v_A^2 k_\perp^2 \rho_i^2}{\beta_i + 2/(1 + T_e/T_i)}, \quad (1)$$

and the oblique whistler wave,

$$\omega^2 = k_\parallel^2 v_A^2 k_\perp^2 d_i^2. \quad (2)$$

To distinguish these, the correlation between δn and $\delta B_\parallel$ can be used, which is negative for the kinetic Alfvén wave and positive for the whistler wave. Figure 3 shows the magnitude-squared wavelet coherence, γ, between δn_e and $\delta B_\parallel$, and the phase lag ϕ (black arrows) for $\gamma > 0.5$, measured by *MMS3*. To avoid complications with the definition of $\boldsymbol{B}_0$, $\delta|\boldsymbol{B}|$ was used as a proxy for $\delta B_\parallel$, which requires $\delta\boldsymbol{B}^2/B_0^2 \ll 2\delta B_\parallel/B_0$, a condition well-satisfied here. For spacecraft-frame frequencies 0.5 Hz $\lesssim f_{sc} \lesssim$ 5 Hz, corresponding to $1 \lesssim k_\perp \rho_i \lesssim 10$, $\gamma \sim 1$ and there is a strong anti-correlation. The average phase lag in this range is $\langle\phi\rangle = (172 \pm 7)^\circ$ (where the uncertainty is the standard deviation). For $f_{sc} \gtrsim 10$ Hz, the anti-correlation is lost due to noise in the density measurement. This strong anti-correlation, along with the $k_\perp \gg k_\parallel$ anisotropy, indicates the predominantly kinetic Alfvén nature of the turbulence in the first decade of the kinetic range.

Figure 4 shows the spectra of various quantities measured by *MMS3*, calculated using the multitaper method (Percival & Walden 1993). In the range $1/\rho_i < k < 1/d_e$, the trace magnetic fluctuation spectrum has a power-law index of -2.8 before steepening at electron scales, similar to solar wind observations (e.g., Alexandrova et al. 2009; Kiyani et al. 2009; Chen et al. 2010a, 2012; Sahraoui et al. 2013) and kinetic Alfvén turbulence simulations (e.g., Howes et al. 2011; Boldyrev & Perez 2012), and not far from the $k_\perp^{-8/3}$ prediction for intermittent kinetic Alfvén turbulence (Boldyrev & Perez 2012). The trace electric field spectrum, Lorentz

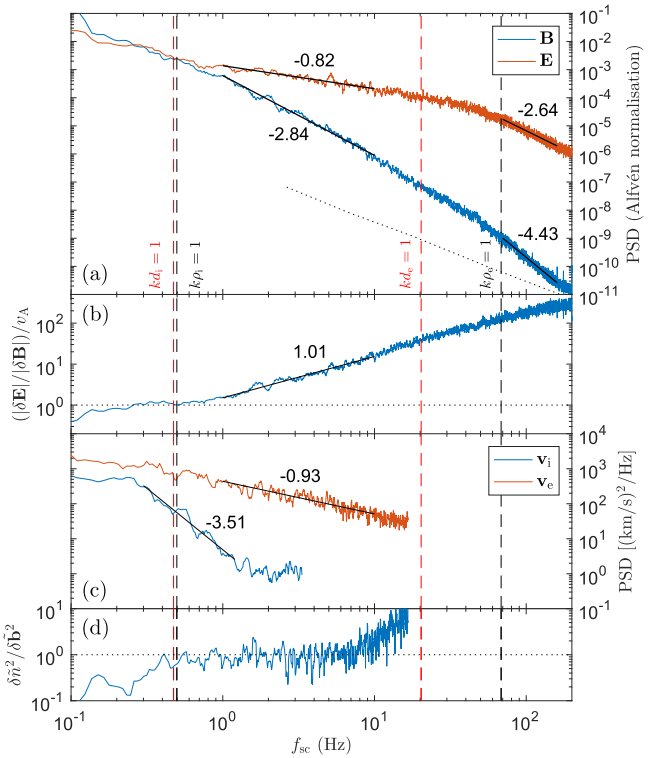


Figure 4. (a) Magnetic field, $\boldsymbol{B}$, and electric field, $\boldsymbol{E}$, power spectra. (b) Ratio of electric and magnetic fluctuations. (c) Ion velocity, $\boldsymbol{v}_i$, and electron velocity, $\boldsymbol{v}_e$, power spectra. (d) Ratio of density and magnetic fluctuations (Equation (3)). The dashed lines mark the plasma microscales under the Taylor hypothesis; the dotted line is the normalized SCM noise floor (Le Contel et al. 2016).

transformed into the zero mean velocity frame (Chen et al. 2011), has a spectral index of -0.8, a factor of k^2 shallower than the magnetic spectrum, before also steepening at electron scales. The ratio $(|\delta\boldsymbol{B}|/|\delta\boldsymbol{E}|)/v_A$ is around unity for $k\rho_i < 1$ then displays linear scaling for $k\rho_i > 1$, as also seen by Matteini et al. (2017). This is because kinetic Alfvén fluctuations, although electromagnetic in nature, have a significant potential component of the electric field; the ion motion satisfies $\omega \ll k_\perp v_{th,i}$, so the density adjusts to the electric potential as $\delta n \propto \phi$, and since $\delta n \propto \delta B$, the electric field is given by $E(k) \approx -ik\phi(k) \propto kB(k)$. The electron velocity spectral index is -0.9, close to k^2 shallower than the magnetic field and similar to the electric field, since the electron velocity is dominated by the $\boldsymbol{E} \times \boldsymbol{B}_0$ drift. The ion velocity spectrum, however, is much steeper, similar to in the upstream solar wind (Šafránková et al. 2013, 2016), reaching the instrumental noise around $k\rho_i \approx 3$. This is because the ions no longer participate in the same $\boldsymbol{E} \times \boldsymbol{B}_0$ drift as the electrons, since their gyroradius is much larger than the scales of the electric field fluctuations in this range. Figure 4(d) shows the normalized ratio of density and magnetic fluctuations,

$$\frac{\delta\tilde{n}^2}{\delta\tilde{\boldsymbol{b}}^2} = \frac{\beta_i}{2}\left(1 + \frac{T_e}{T_i}\right)\left[1 + \frac{\beta_i}{2}\left(1 + \frac{T_e}{T_i}\right)\right]\frac{(\delta n/n_0)^2}{(\delta\boldsymbol{B}/B_0)^2}, \quad (3)$$

which is $\delta\tilde{n}^2/\delta\tilde{\boldsymbol{b}}^2 \sim 1$, confirming that the turbulence is predominantly low frequency, $\omega \ll k_\perp v_{th,i}$, and kinetic Alfvén rather than whistler (Boldyrev et al. 2013; Chen et al. 2013b). The increase in $\delta\tilde{n}^2/\delta\tilde{\boldsymbol{b}}^2$ for $f_{sc} \gtrsim 10$ Hz is not physical, but due to the density spectrum reaching the noise level.

2.3. Nature of Fluctuations at $kd_e \gtrsim 1$

While the first decade of the magnetosheath kinetic range, $1 \lesssim k\rho_i \lesssim 10$, described in Section 2.2, is similar to that in the upstream solar wind, the nature of the turbulence changes in the second decade. The kinetic Alfvén wave (Equation (1)) is derived assuming $\omega \ll k_\parallel v_{th,e}$; however, it can be seen that (for $T_i \gg T_e$) this breaks down at the scale

$$k_\perp^2 \rho_e^2 \sim \beta_i (2 + \beta_i)(T_e/T_i)^2, \tag{4}$$

about halfway between $k_\perp \rho_i \sim 1$ and $k_\perp \rho_e \sim 1$ for the measured parameters. In the range $k_\parallel v_{th,e} \ll \omega \ll k_\perp v_{th,i}$, the kinetic Alfvén wave transforms into a mode with dispersion relation

$$\omega^2 = \frac{k_\parallel^2 v_A^2 k_\perp^2 \rho_i^2}{\beta_i (1 + k_\perp^2 d_e^2)(1 + 2/\beta_i + k_\perp^2 d_e^2)}, \tag{5}$$

which we call the *inertial kinetic Alfvén wave* (see Appendix A for the derivation). This should be distinguished from the standard inertial Alfvén wave derived under the conditions $\beta_e \ll m_e/m_i$ and $\beta_i \ll 1$ (e.g., Lysak & Lotko 1996), which are not satisfied here. Note also that the term "inertial kinetic Alfvén wave" has occasionally been applied to the standard inertial Alfvén wave (Shukla et al. 2009; Agarwal et al. 2011), although the conditions assumed in these works are essentially the same as in Lysak & Lotko (1996) and different from those leading to Equation (5).

The key observational feature of the transition to inertial kinetic Alfvén turbulence is the magnetic compressibility,

$$\frac{\delta B_\parallel^2}{\delta B_\perp^2} = \frac{1 + k_\perp^2 d_e^2}{1 + 2/\beta_i + k_\perp^2 d_e^2}. \tag{6}$$

For $k_\perp^2 d_e^2 \ll 1$, $\delta B_\parallel^2/\delta B_\perp^2 = 1/(1 + 2/\beta_i)$, and for $k_\perp^2 d_e^2 \gg 1 + 2/\beta_i$, $\delta B_\parallel^2/\delta B_\perp^2 = 1$, i.e., in general, the magnetic compressibility increases as energy cascades through $k_\perp d_e \sim 1$. This is because for $k_\perp d_e < 1$, the ion pressure reduces plasma compressibility, which due to pressure balance causes a β_i-dependent reduction in $\delta B_\parallel$. For $k_\perp d_e > 1$, however, the compressibility caused by the electron polarization drift becomes stronger than the compressibility due to the $\boldsymbol{E} \times \boldsymbol{B}$ drift, leading to $\delta B_\parallel^2/\delta B_\perp^2 = 1$.

Figure 5 shows the spectra of $B_\perp$ and $B_\parallel$, and the ratio of these, as measured by *MMS3*. As for Section 2.2, $\delta|\boldsymbol{B}|$ was used as a proxy for $\delta B_\parallel$, and $\delta B_\perp^2 = \delta \boldsymbol{B}^2 - \delta B_\parallel^2$. It can be seen that at $k\rho_i \sim 1$, the magnetic compressibility is $\approx 1/(1 + 2/\beta_i)$, then this increases through $kd_e \sim 1$, becoming ≈ 1 by the time $k\rho_e \sim 1$ is reached. In fact, the red line shows the measured compressibility to be following Equation (6) over the whole range between the ion and electron gyroscales. Note that the increase in compressibility is not due to noise; random fluctuations would produce equal power in all three components, resulting in $\delta B_\parallel^2/\delta B_\perp^2 = 0.5$ (which occurs only for $f_{sc} > 200$ Hz, where the noise level is reached). It is also not due to parallel propagating whistler wave packets, which would appear as enhancements in the spectrum with a strong circular polarization (Matteini et al. 2017), but are not present in this interval. The observed magnetic compressibility, therefore, is consistent with a transition to inertial kinetic Alfvén turbulence for $kd_e \gtrsim 1$.

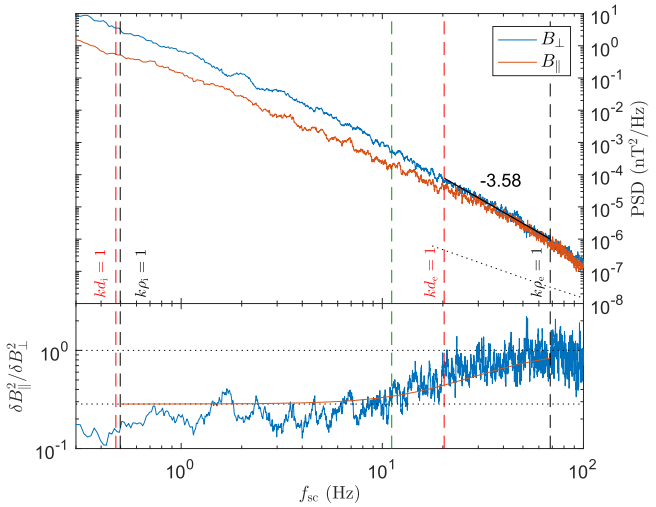


Figure 5. Power spectra of $B_\perp$ and $B_\parallel$ and magnetic compressibility $\delta B_\parallel^2/\delta B_\perp^2$. In the lower panel, the black dotted lines show the asymptotic predictions $1/(1 + 2/\beta_i)$ and 1, and the red solid line is Equation (6). The vertical dashed lines are the same as in Figure 4; the additional green line is the transition scale (Equation (4)).

2.4. Validity of the Taylor Hypothesis

The use of the Taylor hypothesis to interpret Figures 2–5 in the spatial domain requires careful consideration. This assumes that the plasma-frame frequencies are small compared to the frequency of the convected spatial variations $|\omega| \ll |\boldsymbol{k} \cdot \boldsymbol{v}|$. If the fluctuations follow the kinetic Alfvén wave (Equation (1)) and inertial kinetic Alfvén wave (Equation (5)) dispersion relations, which the measurements of Sections 2.2 and 2.3 are consistent with, this condition (for $T_i \gg T_e$) becomes $k_\parallel \rho_i \ll (v/v_A)\sqrt{\beta_i(1 + k_\perp^2 d_e^2)(1 + 2/\beta_i + k_\perp^2 d_e^2)}$ (see also Howes et al. 2014). For $k_\perp^2 d_e^2 \ll 1$, this reduces to $k_\parallel \rho_i \ll (v/v_A)\sqrt{2 + \beta_i} \approx 1.3$. Due to the anisotropy $k_\perp \gg k_\parallel$, this can be well-satisfied, even for $k_\perp \rho_i \gg 1$. For $k_\perp^2 d_e^2 \gg 1 + 2/\beta_i$ this reduces to $k_\parallel \rho_i \ll (v/v_A)\sqrt{\beta_i} k_\perp^2 d_e^2$, which can be written $k_\parallel/k_\perp \ll k_\perp v/\Omega_e$. Therefore, as long as $k_\parallel/k_\perp$ does not grow faster than $k_\perp$ (theoretical considerations suggest it actually grows more slowly; see Section 3.2), the Taylor condition would remain valid down to $k_\perp \rho_e \sim 1$.

A recent numerical study (Klein et al. 2014) concluded that the Taylor hypothesis is indeed satisfied for kinetic Alfvén turbulence at $v/v_A \sim 1$ and if it was violated significantly shallower spectra would result. The fact that the spectra in Figure 4 match those in the solar wind, as well as expectations from simulations and theory, is consistent with the interpretation that the measured fluctuations are spatial. As a more direct test, Figure 6 shows the normalized magnetic fluctuation amplitudes, as calculated from the second-order structure function, from both the single-spacecraft method (converting from the temporal to spatial domain assuming the Taylor hypothesis) and as direct spatial measurements from the six pairs of *MMS* spacecraft. There is some scatter in the multi-spacecraft measurements, due to the spacecraft separation vectors being at different angles to the mean field direction, but the average value of $|\delta \boldsymbol{B}|/B_0 = 0.018$ is similar to the single-spacecraft value of $|\delta \boldsymbol{B}|/B_0 = 0.019$, consistent with the Taylor hypothesis being valid down to $kd_e \sim 1$.

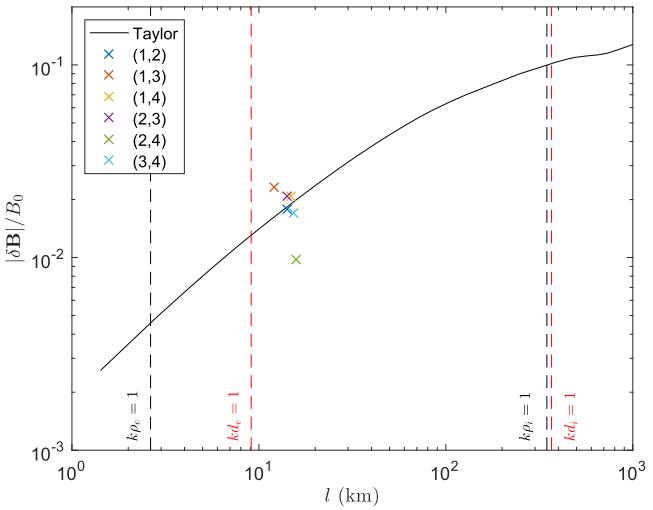


Figure 6. Normalized magnetic fluctuation amplitude $|\delta\boldsymbol{B}|/B_0$ as a function of scale l measured with the single-spacecraft method assuming the Taylor hypothesis (black line), and with pairs of spacecraft (i, j) as a direct spatial measurement. The vertical dashed lines are the same as in Figure 4.

3. Theoretical Model

3.1. Dynamical Equations for Inertial Kinetic Alfvén Turbulence

To understand the nonlinear properties of the cascade, we first derive the dynamical equations for inertial kinetic Alfvén turbulence. We consider strongly anisotropic ($k_\perp \gg k_\parallel$) fluctuations, and use the ordering $k_\parallel/k_\perp \sim \delta B/B_0 \sim \delta n/n_0 \sim \omega/\Omega_e \ll 1$.

The starting equations are the electron continuity and momentum equations. In the electron continuity equation,

$$\frac{\partial n}{\partial t} + \nabla_\perp \cdot (n\boldsymbol{v}_\perp) + \nabla_\parallel (nv_\parallel) = 0, \tag{7}$$

the parallel electron velocity can be expressed through the parallel electron current, $v_\parallel = -J_\parallel/(ne)$, which can, in turn, be expressed through the z component of the magnetic vector potential, $\psi \equiv -A_z \approx -A_\parallel$, as $J_\parallel = (1/\mu_0)\nabla_\perp^2\psi$. Here, e is the magnitude of the electron charge. Due to the small amplitude of the magnetic fluctuations, $\delta B/B_0 \ll 1$, the deviation of the magnetic field lines from the z direction (large-scale mean field) is small, so the parallel components of the vector fields can be approximated by their z components. This is, however, not true for the parallel gradients, since $k_\parallel \ll k_\perp$, which are given by

$$\nabla_\parallel = \partial/\partial z + B_0^{-1}(\hat{z} \times \nabla\psi) \cdot \nabla. \tag{8}$$

The perpendicular electron velocity is more complicated. It has two parts, the $\boldsymbol{E} \times \boldsymbol{B}$ drift and the polarization drift,

$$\boldsymbol{v}_\perp = \boldsymbol{v}_E - \frac{m_e}{eB^2}\boldsymbol{B} \times \frac{d_E}{dt}\boldsymbol{v}_E. \tag{9}$$

In this expression, $\boldsymbol{v}_E = (\boldsymbol{E} \times \boldsymbol{B})/B^2$ is the $\boldsymbol{E} \times \boldsymbol{B}$ drift velocity, the convective derivative is $d_E/dt \equiv \partial/\partial t + \boldsymbol{v}_E \cdot \nabla$, and we note that $B^2 \approx B_0^2 + 2B_0\delta B_z$. The second term on the right-hand side of Equation (9) is smaller than the first by ω/Ω_e; however, it needs to be retained since in the continuity equation the leading contribution from the first term cancels out. The electric field has both potential and non-potential components, $\boldsymbol{E} = -\nabla\phi + \boldsymbol{E}_{np}$. The non-potential component is small compared to the potential one as it includes the (small) time derivative of the (small) magnetic fluctuations,

$$\nabla \times \boldsymbol{E}_{np} = -\frac{\partial \delta\boldsymbol{B}}{\partial t}, \tag{10}$$

although it also needs to be retained for the same reason. The fluctuations of the perpendicular magnetic field component are given by the z component of the magnetic vector potential, $\delta\boldsymbol{B}_\perp = \hat{z} \times \nabla\psi$.

Substituting these expressions into Equation (7), and keeping the leading order terms, we obtain

$$\frac{\partial}{\partial t}\left(\frac{\delta n}{n_0} - \frac{\delta B_z}{B_0} + \frac{m_e}{eB_0^2}\nabla^2\phi\right) + \frac{1}{B_0}(\hat{z} \times \nabla\phi) \cdot \nabla\left(\frac{\delta n}{n_0} - \frac{\delta B_z}{B_0} + \frac{m_e}{eB_0^2}\nabla^2\phi\right) - \frac{1}{\mu_0 n_0 e}\nabla_\parallel\nabla_\perp^2\psi = 0. \tag{11}$$

We now turn to the electron momentum equation. The parallel component of the equation is

$$\frac{\partial v_\parallel}{\partial t} + (\boldsymbol{v}_E \cdot \nabla)v_\parallel = -\frac{e}{m_e}E_\parallel - \frac{1}{m_e n}\nabla_\parallel p_e. \tag{12}$$

Here, we have made use of $k_\perp \gg k_\parallel$ and $v_\parallel \sim v_\perp$. The latter condition can be checked a posteriori from the expressions for the parallel and perpendicular velocity components. The electric field is expressed through the scalar and vector potentials,

$$E_\parallel = -\nabla_\parallel\phi - \partial A_\parallel/\partial t. \tag{13}$$

As can be checked, the electron pressure fluctuations can be neglected compared to the electric potential fluctuations, ϕ, for $T_e \ll T_i$. We then get the equation for the z component of the magnetic potential ψ,

$$\frac{\partial}{\partial t}(\psi - d_e^2\nabla_\perp^2\psi) - d_e^2(\boldsymbol{v}_E \cdot \nabla)\nabla_\perp^2\psi = \nabla_\parallel\phi. \tag{14}$$

To close Equations (11) and (14), we need to find two additional relations among the fluctuating fields. One of these can be found from the perpendicular component of the electron momentum equation. Neglecting the small electron pressure, the force balance in the perpendicular direction is

$$\boldsymbol{E}_\perp + \boldsymbol{v}_\perp \times \boldsymbol{B} = 0. \tag{15}$$

Writing the perpendicular velocity as $\boldsymbol{v}_\perp = -\boldsymbol{J}_\perp/(ne) = -(\nabla \times \boldsymbol{B})_\perp/(\mu_0 ne)$, the electric field is then given by

$$\boldsymbol{E}_\perp \approx [(\boldsymbol{B} \cdot \nabla)\delta\boldsymbol{B}_\perp - B_0\nabla_\perp\delta B_z]/(\mu_0 ne). \tag{16}$$

Since, as we will see later, $\delta B_z \sim \delta B_\perp$, the first term on the right-hand side of Equation (16) is small. Using $k_\perp \gg k_\parallel$, the relation between the electric potential and the z component of the fluctuating magnetic field is obtained,

$$\phi = \frac{B_0}{\mu_0 ne}\delta B_z. \tag{17}$$

For the second relation, we use the fact that kinetic Alfvén fluctuations exist for $\omega \ll kv_{th,i}$. In this case, the ion (and, by

quasineutrality, electron) density fluctuations adjust to the electric potential according to the Boltzmann formula,

$$\phi = -\frac{T_i}{e}\frac{\delta n}{n_0}. \quad (18)$$

It can be seen that Equations (17) and (18) agree with the force balance in the single-fluid momentum equation, $\delta B_z/B_0 = -(\beta_i/2)(\delta n/n_0)$. We can now eliminate the δB_z and ϕ fluctuations from Equations (11) and (14) in favor of the density fluctuations. Using the dimensionless variables $t' = t|\Omega_e|$, $\boldsymbol{x}' = \boldsymbol{x}/d_e$, $\psi' = \psi/(d_e B_0)$, $\delta n' = (\beta_i/2)(\delta n/n_0)$, and omitting the prime signs, we obtain the nonlinear system of equations for inertial kinetic Alfvén turbulence:

$$\frac{\partial}{\partial t}(1 - \nabla_\perp^2)\psi + [(\hat{z} \times \nabla\delta n)\cdot\nabla]\nabla_\perp^2\psi = -\nabla_\parallel \delta n, \quad (19)$$

$$\frac{\partial}{\partial t}\left(1 + \frac{2}{\beta_i} - \nabla_\perp^2\right)\delta n + [(\hat{z} \times \nabla\delta n)\cdot\nabla]\nabla_\perp^2\delta n = \nabla_\parallel\nabla_\perp^2\psi. \quad (20)$$

The nonlinearities in these equations appear in the second terms on the left-hand sides, and in the parallel gradients on the right-hand sides,

$$\nabla_\parallel = \partial/\partial z + (\hat{z} \times \nabla\psi)\cdot\nabla. \quad (21)$$

Without the nonlinear terms, these equations reproduce the inertial kinetic Alfvén wave dispersion relation (Equation (36)), and the relation between δn and ψ for these modes,

$$\delta n = \sqrt{\frac{1 + k_\perp^2}{1 + 2/\beta_i + k_\perp^2}}\, k_\perp \psi. \quad (22)$$

The last equation agrees with Equation (6) since $k_\perp\psi$ represents the perpendicular magnetic fluctuations, and $\delta n = -\delta B_z$ in the above normalization.

3.2. Energy Spectrum and Anisotropy

From Equations (19) and (20), we can derive the spectrum of inertial kinetic Alfvén turbulence. In the absence of energy supply and dissipation, the equations conserve the energy

$$E = \int\left[\delta n\left(1 + \frac{2}{\beta_i} - \nabla_\perp^2\right)\delta n - \nabla_\perp^2\psi(1 - \nabla_\perp^2)\psi\right]d^3\boldsymbol{x}. \quad (23)$$

In a turbulent state, both terms of E are of the same order. For scales $k_\perp^2 \gg 1 + 2/\beta_i$, this means that $\delta n_\lambda \sim \psi_\lambda/\lambda$, where δn_λ and ψ_λ denote the typical fluctuations of the fields at the scale λ across the background magnetic field. In the same limit, the nonlinearity is dominated by the terms on the left-hand sides of Equations (19) and (20), and the nonlinear time can be estimated as $\tau \sim \lambda^2/\delta n_\lambda$. Assuming a constant energy flux through scales, $\varepsilon \sim (\delta n_\lambda^2/\lambda^2)/\tau \sim \delta n_\lambda^3/\lambda^4$, leads to the scaling of the density and magnetic fluctuations $\delta n_\lambda \sim \psi_\lambda/\lambda \sim \varepsilon^{1/3}\lambda^{4/3}$. Applying the Fourier transform in the plane perpendicular to the background magnetic field, the spectrum of density and perpendicular fluctuations is obtained, $E_{n,B}(k_\perp) \propto k_\perp^{-11/3}$. In the data interval discussed in Section 2, the scaling range between $kd_e \sim 1$ and $k\rho_i \sim 1$ is not large (a factor of 3.4), so a well-developed power-law spectrum is not present, but the measured spectral index can still be compared to the prediction in the limited range. Figure 5 shows the spectral index to be -3.6 for the $\delta B_\perp$ fluctuations between $kd_e = 1$ and $k\rho_e = 1$, which is not far from the predicted value of $-11/3$.

The anisotropy implied by the critical balance condition can also be determined. Balancing the linear and nonlinear terms in Equations (19) and (20), $\psi_\lambda/(l_\parallel\lambda^2) \sim \delta n_\lambda^2/\lambda^4$, we obtain the relation between the parallel and perpendicular scales $l_\parallel \sim \lambda^{5/3}$. In Fourier space this means that the turbulent energy is concentrated in the region $k_\parallel \lesssim k_\perp^{5/3}$, which becomes progressively broader in $k_\parallel$ and less anisotropic as $k_\perp$ increases. This suggests, therefore, that in contrast to standard Alfvén and kinetic Alfvén turbulence, the energy cascade in inertial kinetic Alfvén turbulence supplies energy more efficiently to $k_\parallel$ rather than $k_\perp$ modes. This anisotropy also implies that the Taylor condition becomes better satisfied as $k_\perp$ increases (see Section 2.4). The current data interval does not allow the scale-dependence of the anisotropy to be tested, but this could be done in future studies with larger data sets, and also tested in numerical simulations.

3.3. Inertial Whistler Turbulence

The condition derived in Section 3.2 that critically balanced inertial kinetic Alfvén turbulence becomes more isotropic toward smaller scales leads to the interesting possibility that the cascade may transition to inertial whistler turbulence if the anisotropy reduces sufficiently. This is because there is a maximum value of $k_\parallel/k_\perp$ at which inertial kinetic Alfvén waves can exist (see Appendix A); the broadening of the spectrum in the $k_\parallel$ direction would lead to the turbulence reaching $\omega > kv_{th,i}$, which is the whistler frequency range.

For completeness, we give here the dynamical equations for inertial whistler turbulence. The basic Equations (11) and (14) hold for whistler turbulence as well; however, the additional condition (18) needs to be modified. Due to the high frequency of the whistlers, the density fluctuations do not follow the electric potential and remain small,

$$\frac{\delta n}{n_0} \ll -\frac{e\phi}{T_i}. \quad (24)$$

We can thus neglect the density fluctuations in Equations (11) and (14), and use Equation (17) to remove the electric potential fluctuations. Using again the normalized variables, and also $\delta B_z' = \delta B_z/B_0$, with the primes omitted, we obtain the nonlinear equations for inertial whistler turbulence:

$$\frac{\partial}{\partial t}(1 - \nabla_\perp^2)\psi - [(\hat{z} \times \nabla\delta B_z)\cdot\nabla]\nabla_\perp^2\psi = \nabla_\parallel\delta B_z, \quad (25)$$

$$\frac{\partial}{\partial t}(1 - \nabla_\perp^2)\delta B_z - [(\hat{z} \times \nabla\delta B_z)\cdot\nabla]\nabla_\perp^2\delta B_z = -\nabla_\parallel\nabla_\perp^2\psi. \quad (26)$$

Linearization of these equations leads to the inertial whistler wave dispersion relation, which (in unnormalized variables) is given by

$$\omega^2 = \frac{k_\parallel^2 v_A^2 k_\perp^2 \rho_i^2}{\beta_i(1 + k_\perp^2 d_e^2)^2}, \quad (27)$$

and is also derived in Appendix B.

Due to the structural similarity of the inertial kinetic Alfvén and inertial whistler equations, (19), (20) and (25), (26), the spectrum of magnetic fluctuations in inertial whistler turbulence is the same as that derived in Section 3.2, with the difference that the transition to the inertial regime occurs at $k_\perp^2 > 1$ rather than $k_\perp^2 > 1 + 2/\beta_i$. This spectrum for inertial whistler turbulence has also been discussed previously (Biskamp et al. 1996, 1999; Meyrand & Galtier 2010; Andrés et al. 2014). The structural similarity between the equations means that the anisotropy implied by the critical balance condition (discussed in Section 3.2) is also the same, meaning that the increasing isotropization would continue if the inertial kinetic Alfvén cascade transitions to inertial whistler turbulence.

The main physical difference between inertial kinetic Alfvén and inertial whistler turbulence is the ion dynamics, as discussed above, which leads to negligibly small density fluctuations in inertial whistler turbulence (see Appendix B). The magnetic compressibility, however, is the same, with $\delta B_\perp^2/\delta B_\parallel^2 = 1$ for both types of turbulence at sub-electron-inertial scales. The measurements in Figure 5, therefore, allow for the possibility of a transition to inertial whistler turbulence between $kd_e \sim 1$ and $k\rho_e \sim 1$. Further measurements will be required to determine whether, and under what conditions, such a transition occurs.

4. Discussion

We have presented measurements of kinetic scale turbulence in the Earth's magnetosheath, which have the conditions $T_i \gg T_e$ and $\beta_i \sim 1$. In the first decade of the kinetic range, the turbulence is similar to that in the upstream solar wind: it is predominantly low-frequency ($\omega \ll k_\perp v_{th,i}$), anisotropic ($k_\perp \gg k_\parallel$), and kinetic Alfvén in nature, with spectra that match theoretical predictions and numerical simulations. In the second decade, however, a regime of inertial kinetic Alfvén turbulence has been identified by the increase in magnetic compressibility following that of the inertial kinetic Alfvén wave (Equation (6)). A set of nonlinear equations (Equations (19)–(20)) has been derived, which can be used to obtain the spectrum of magnetic fluctuations, $E_B(k_\perp) \propto k_\perp^{-11/3}$, between the electron inertial scale and electron gyroscale, which is consistent with the observed spectral steepening. Interestingly, this turbulence is expected to exhibit a qualitatively different scale-dependent anisotropy to standard Alfvén and kinetic Alfvén turbulence, becoming less anisotropic toward smaller scales. This increasing isotropization may lead to a transition to inertial whistler turbulence (described by Equations (25) and (26)) if the frequency reaches $\omega > k_\perp v_{th,i}$. We plan to investigate these aspects with further observations and numerical simulations.

As well as in the Earth's magnetosheath, inertial kinetic Alfvén turbulence may also be present in several other astrophysical environments, with comparable plasma parameters. For example, the fast solar wind model of Chandran et al. (2011) predicts $\beta_i \sim 0.1$ and $\beta_e \sim 0.02$ at 10 solar radii from the Sun, a regime in which inertial kinetic Alfvén turbulence would be expected to constitute a significant fraction of the kinetic range. This region of the solar corona will soon be measured in situ by the *Solar Probe Plus* spacecraft (Fox et al. 2016), allowing this to be tested directly. Similarly, in hot accretion flows, where turbulent heating is thought to be important, the ions are likely to be hotter than the electrons (Quataert 1998), allowing the possibility of inertial kinetic Alfvén turbulence at small scales. Finally, collisionless shocks, such as the one that generates the Earth's magnetosheath, are common throughout the universe, leading to turbulent regions of space with large T_i/T_e (Treumann 2009; Ghavamian et al. 2013). Inertial kinetic Alfvén turbulence, therefore, may be quite widespread, and a possible route through which astrophysical plasmas are heated.

C.H.K.C. is supported by an STFC Ernest Rutherford Fellowship. S.B. is supported by the Space Science Institute, NSF grant AGS-1261659, and by the Vilas Associates Award from UW Madison. We acknowledge the *MMS* team for producing the data, which were obtained from the *MMS* Science Data Center (https://lasp.colorado.edu/mms/sdc/).

Appendix A
Derivation of the Inertial Kinetic Alfvén Wave

In a $\beta \sim 1$ plasma, when the wave propagation is oblique, $k_\perp \gg k_\parallel$, the Alfvén wave transforms into the kinetic Alfvén wave for scales $k_\perp \rho_i > 1$. The situation is different, however, when either β_i or β_e is small. In the regime of extremely small electron plasma beta $\beta_e \ll m_e/m_i$, and $\beta_i \ll 1$, the Alfvén wave transforms into the inertial Alfvén wave (e.g., Lysak & Lotko 1996). In this case, the electron thermal velocity is much smaller than the Alfvén velocity, and the electrons do not adjust instantaneously to the electric field acting along the magnetic field lines. The regime here, however, is different, $m_e/m_i \ll \beta_e \ll 1$, and the standard inertial Alfvén theory does not apply.

The dispersion relation for the standard kinetic Alfvén wave (e.g., Howes et al. 2006), derived under the assumption $\omega \ll k_z v_{th,e}$, is

$$\omega^2 = \frac{k_z^2 v_A^2 k_\perp^2 \rho_i^2 (1 + T_e/T_i)}{2 + \beta_i (1 + T_e/T_i)} \approx \frac{k_z^2 v_A^2 k_\perp^2 \rho_i^2}{2 + \beta_i}, \tag{28}$$

where $T_e \ll T_i$ has been assumed in the last expression. Note that in the linear theory, the global and local mean magnetic field directions are the same, and here we use z for this direction. It can be seen, however, that the frequency of the kinetic Alfvén wave becomes larger than $k_z v_{th,e}$ for

$$k_\perp^2 \rho_e^2 > \beta_i (2 + \beta_i)(T_e/T_i)^2. \tag{29}$$

For $T_e \ll T_i$ and $\beta_i \sim 1$, this happens at a scale much larger than the electron gyroscale.

In the frequency range $k_z v_{th,e} \ll \omega \ll k_\perp v_{th,i}$, the kinetic Alfvén wave transforms into the inertial kinetic Alfvén wave. To derive this mode, we consider a collisionless plasma with $\beta_i \lesssim 1$, at sub-ion scales $k_\perp \rho_i \gg 1$. The wave modes can be found from the equation $D_{ij} E_j = 0$, where $D_{ij} = k^2 \delta_{ij} - k_i k_j - (\omega^2/c^2)\epsilon_{ij}$, ϵ_{ij} is the plasma dielectric tensor, and E_j is the electric field. Under the additional assumption $T_e \ll T_i$, the components of the tensor D_{ij} take the form

$$D_{xx} \approx k_z^2 - \frac{\omega^2}{c^2}\frac{\omega_{pe}^2}{\Omega_e^2}\left(1 + \frac{2}{\beta_i k_\perp^2 d_i^2}\right), \tag{30}$$

$$D_{xy} = -D_{yx} \approx -i\frac{\omega\omega_{pe}^2}{\Omega_e c^2}, \tag{31}$$

$$D_{xz} = D_{zx} \approx -k_z k_\perp, \tag{32}$$

$$D_{yy} \approx k^2, \tag{33}$$

$$D_{zz} \approx k_\perp^2 + \frac{\omega_{pe}^2}{c^2}, \tag{34}$$

$$D_{yz} = D_{zy} \approx 0, \tag{35}$$

where the wave vector has components $(k_\perp, 0, k_z)$.

The dispersion relation for the inertial kinetic Alfvén wave obtained from this equation is

$$\omega^2 = \frac{k_z^2 k_\perp^2 d_e^4 \Omega_e^2}{(1 + k_\perp^2 d_e^2)(1 + 2/\beta_i + k_\perp^2 d_e^2)}. \tag{36}$$

When the electron inertial corrections are small, $k_\perp^2 d_e^2 \ll 1$, this is similar to the dispersion relation of the standard kinetic Alfvén wave (Equation (28)), although in a different phase space region, $\omega \gg k_z v_{th,e}$, which indicates that the dispersion relation is not sensitive to $\omega/(k_z v_{th,e})$. In the opposite case, $k_\perp^2 d_e^2 \gg 1 + 2/\beta_i$, the inertial kinetic Alfvén wave frequency becomes

$$\omega^2 = \Omega_e^2 k_z^2 / k_\perp^2. \tag{37}$$

A similar derivation for the Alfvén modes at low β can also be made starting from the gyrokinetic description (e.g., Howes et al. 2006; Zocco & Schekochihin 2011).

The inertial kinetic Alfvén wave exists for $\omega^2 \ll k_\perp^2 v_{th,i}^2$, which, together with the dispersion relation (Equation (36)), allows the required obliquity to be determined. At $k_\perp^2 d_e^2 \sim 1$ the wave requires $k_z^2/k_\perp^2 \ll m_e/m_i$, and at $k_\perp^2 \rho_e^2 \sim 1$ the condition is $k_z^2/k_\perp^2 \ll (m_e/m_i)(T_i/T_e)$.

The density fluctuations associated with the inertial kinetic Alfvén wave are

$$\left(\frac{\delta n}{n_0}\right)^2 = \frac{4}{\beta_i^2}\left(1 + \frac{1 + 2/\beta_i + k_\perp^2 d_e^2}{1 + k_\perp^2 d_e^2}\right)^{-1}\left(\frac{\delta \boldsymbol{B}}{B_0}\right)^2, \tag{38}$$

and they are anti-correlated with the fluctuations of the magnetic field strength,

$$\frac{\delta B_z}{B_0} = -\frac{\beta_i}{2}\frac{\delta n}{n_0}. \tag{39}$$

From Equations (38) and (39), the expression for the magnetic compressibility is obtained,

$$\frac{\delta B_z^2}{\delta B_\perp^2} = \frac{1 + k_\perp^2 d_e^2}{1 + 2/\beta_i + k_\perp^2 d_e^2}. \tag{40}$$

Appendix B
Derivation of the Inertial Whistler Wave

The whistler wave, unlike the kinetic Alfvén wave, exists for frequencies $\omega > k_\perp v_{th,i}$ and transforms into the inertial whistler wave at $k_\perp d_e \sim 1$. It can be derived from the same Equations (30)–(35), if D_{xx} is replaced by

$$D_{xx} = k_z^2 - \frac{\omega^2\omega_{pe}^2}{c^2\Omega_e^2} + \frac{\omega_{pi}^2}{c^2}. \tag{41}$$

The dispersion relation for the inertial whistler wave is then obtained,

$$\omega^2 = k_z^2 k^2 d_e^4 \Omega_e^2 \frac{\left[1 + \frac{1 + k_\perp^2 d_e^2}{k_z^2 d_i^2}\right]}{(1 + k^2 d_e^2)(1 + k_\perp^2 d_e^2)}. \tag{42}$$

Without the electron inertial corrections, $kd_e \ll 1$, the wave exists only for $k_z d_i \gg 1$, where we recover the well-known whistler dispersion relation. In the opposite limit, $k_\perp d_e \gg 1$, the whistlers exist for $k_z d_i \gg k_\perp^2 d_e^2$, so the second term in the square bracket in Equation (42) can always be neglected. Equation (42) then matches the previously studied whistler wave in the inertial regime (e.g., Biskamp et al. 1996, 1999).

The density fluctuations associated with the inertial whistler wave are given by

$$\left(\frac{\delta n}{n_0}\right)^2 = \frac{(1 + k_\perp^2 d_e^2)^4}{(1 + k_z^2 d_i^2 + k_\perp^2 d_e^2)^2\left[1 + \frac{k_z^2 d_i^2}{1 + k_z^2 d_i^2 + k_\perp^2 d_e^2}\right]}\left(\frac{\delta \boldsymbol{B}}{B_0}\right)^2, \tag{43}$$

and are positively correlated with the fluctuations of the magnetic field strength,

$$\frac{\delta n}{n_0} = \frac{(1 + k_\perp^2 d_e^2)^2}{1 + k_\perp^2 d_e^2 + k_z^2 d_i^2}\frac{\delta B_z}{B_0}. \tag{44}$$

For $kd_e \ll 1$, the wave satisfies $k_z d_i \gg 1$ and we recover the well-known relation, $(\delta n/n_0)^2/(\delta B_z/B_0)^2 = 1/(k_z^4 d_i^4)$. In the inertial regime $k_\perp d_e \gg 1$ it satisfies $k_z d_i \gg k_\perp^2 d_e^2$, and we obtain $(\delta n/n_0)^2/(\delta B_z/B_0)^2 = (k_\perp^4 d_e^4)^2/(k_z^2 d_i^2)^2$. In both cases, the density fluctuations are much smaller than the magnetic fluctuations. Also, in both cases the magnetic compressibility is given by

$$\frac{\delta B_z^2}{\delta B_\perp^2} = 1. \tag{45}$$

References

Agarwal, P., Varma, P., & Tiwari, M. S. 2011, P&SS, 59, 306
Alexandrova, O., Chen, C. H. K., Sorriso-Valvo, L., Horbury, T. S., & Bale, S. D. 2013, SSRv, 178, 101
Alexandrova, O., Lacombe, C., & Mangeney, A. 2008, AnGeo, 26, 3585
Alexandrova, O., Saur, J., Lacombe, C., et al. 2009, PhRvL, 103, 165003
Andrés, N., Gonzalez, C., Martin, L., Dmitruk, P., & Gómez, D. 2014, PhPl, 21, 122305
Bale, S. D., Kellogg, P. J., Mozer, F. S., Horbury, T. S., & Reme, H. 2005, PhRvL, 94, 215002
Biskamp, D., Schwarz, E., & Drake, J. F. 1996, PhRvL, 76, 1264
Biskamp, D., Schwarz, E., Zeiler, A., Celani, A., & Drake, J. F. 1999, PhPl, 6, 751
Boldyrev, S., Horaites, K., Xia, Q., & Perez, J. C. 2013, ApJ, 777, 41
Boldyrev, S., & Perez, J. C. 2012, ApJL, 758, L44
Boldyrev, S., Perez, J. C., Borovsky, J. E., & Podesta, J. J. 2011, ApJL, 741, L19
Boldyrev, S., Perez, J. C., & Wang, Y. 2012, in ASP Conf. Ser. 459, Numerical Modeling of Space Plasma Flows, ed. N. V. Pogorelov et al. (San Francisco, CA: ASP), 3

Bruno, R., & Carbone, V. 2013, LRSP, 10, 2
Bruno, R., & Telloni, D. 2015, ApJL, 811, L17
Burch, J. L., Moore, T. E., Torbert, R. B., & Giles, B. L. 2016, SSRv, 199, 5
Burgess, D., & Scholer, M. 2013, SSRv, 178, 513
Cerri, S. S., Califano, F., Jenko, F., Told, D., & Rincon, F. 2016, ApJL, 822, L12
Chandran, B. D. G., Dennis, T. J., Quataert, E., & Bale, S. D. 2011, ApJ, 743, 197
Chaston, C., Bonnell, J., McFadden, J. P., et al. 2008, GeoRL, 35, L17S08
Chen, C. H. K. 2016, JPlPh, 82, 535820602
Chen, C. H. K., Bale, S. D., Salem, C., & Mozer, F. S. 2011, ApJL, 737, L41
Chen, C. H. K., Bale, S. D., Salem, C. S., & Maruca, B. A. 2013a, ApJ, 770, 125
Chen, C. H. K., Boldyrev, S., Xia, Q., & Perez, J. C. 2013b, PhRvL, 110, 225002
Chen, C. H. K., Horbury, T. S., Schekochihin, A. A., et al. 2010a, PhRvL, 104, 255002
Chen, C. H. K., Howes, G. G., Bonnell, J. W., et al. 2013c, in AIP Conf. Proc. 1539, Solar Wind 13, ed. G. P. Zank et al. (Melville, NY: AIP), 143
Chen, C. H. K., Salem, C. S., Bonnell, J. W., Mozer, F. S., & Bale, S. D. 2012, PhRvL, 109, 035001
Chen, C. H. K., Wicks, R. T., Horbury, T. S., & Schekochihin, A. A. 2010b, ApJL, 711, L79
Cho, J., & Lazarian, A. 2004, ApJL, 615, L41
Czaykowska, A., Bauer, T. M., Treumann, R. A., & Baumjohann, W. 2001, AnGeo, 19, 275
Dudok de Wit, T., & Krasnosel'skikh, V. V. 1996, NPGeo, 3, 262
Ergun, R. E., Tucker, S., Westfall, J., et al. 2016, SSRv, 199, 167
Fox, N. J., Velli, M. C., Bale, S. D., et al. 2016, SSRv, 204, 7
Franci, L., Verdini, A., Matteini, L., Landi, S., & Hellinger, P. 2015, ApJL, 804, L39
Ghavamian, P., Schwartz, S. J., Mitchell, J., Masters, A., & Laming, J. M. 2013, SSRv, 178, 633
Goldreich, P., & Sridhar, S. 1995, ApJ, 438, 763
Goldstein, M. L., Wicks, R. T., Perri, S., & Sahraoui, F. 2015, RSPTA, 373, 20140147
He, J., Marsch, E., Tu, C.-Y., Yao, S., & Tian, H. 2011, ApJ, 731, 85
Howes, G. G., Bale, S. D., Klein, K. G., et al. 2012, ApJL, 753, L19
Howes, G. G., Cowley, S. C., Dorland, W., et al. 2006, ApJ, 651, 590
Howes, G. G., Cowley, S. C., Dorland, W., et al. 2008, JGR, 113, 5103
Howes, G. G., Klein, K. G., & TenBarge, J. M. 2014, ApJ, 789, 106
Howes, G. G., & Quataert, E. 2010, ApJL, 709, L49
Howes, G. G., TenBarge, J. M., Dorland, W., et al. 2011, PhRvL, 107, 035004
Huang, S. Y., Sahraoui, F., Deng, X. H., et al. 2014, ApJL, 789, L28
Kiyani, K. H., Chapman, S. C., Khotyaintsev, Y. V., Dunlop, M. W., & Sahraoui, F. 2009, PhRvL, 103, 075006
Kiyani, K. H., Chapman, S. C., Sahraoui, F., et al. 2013, ApJ, 763, 10
Klein, K. G., Howes, G. G., TenBarge, J. M., et al. 2012, ApJ, 755, 159
Klein, K. G., Howes, G. G., & TenBarge, J. M. 2014, ApJL, 790, L20
Krasnoselskikh, V., Balikhin, M., Walker, S. N., et al. 2013, SSRv, 178, 535
Le Contel, O., Leroy, P., Roux, A., et al. 2016, SSRv, 199, 257
Lindqvist, P.-A., Olsson, G., Torbert, R. B., et al. 2016, SSRv, 199, 137
Lucek, E. A., Constantinescu, D., Goldstein, M. L., et al. 2005, SSRv, 118, 95
Lysak, R. L., & Lotko, W. 1996, JGR, 101, 5085
Mangeney, A., Lacombe, C., Maksimovic, M., et al. 2006, AnGeo, 24, 3507
Matteini, L., Alexandrova, O., Chen, C. H. K., & Lacombe, C. 2017, MNRAS, 466, 945
Meyrand, R., & Galtier, S. 2010, ApJ, 721, 1421
Percival, D. B., & Walden, A. T. 1993, Spectral Analysis for Physical Applications (Cambridge: Cambridge Univ. Press)
Podesta, J. J., & Gary, S. P. 2011, ApJ, 734, 15
Pollock, C., Moore, T., Jacques, A., et al. 2016, SSRv, 199, 331
Quataert, E. 1998, ApJ, 500, 978
Russell, C. T., Anderson, B. J., Baumjohann, W., et al. 2016, SSRv, 199, 189
Šafránková, J., Němeček, Z., Němec, F., et al. 2016, ApJ, 825, 121
Šafránková, J., Němeček, Z., Přech, L., & Zastenker, G. N. 2013, PhRvL, 110, 025004
Sahraoui, F., Goldstein, M. L., Robert, P., & Khotyaintsev, Y. V. 2009, PhRvL, 102, 231102
Sahraoui, F., Huang, S. Y., Belmont, G., et al. 2013, ApJ, 777, 15
Schekochihin, A. A., Cowley, S. C., Dorland, W., et al. 2009, ApJS, 182, 310
Shukla, N., Varma, P., & Tiwari, M. S. 2009, IJPAP, 47, 350
Stawarz, J. E., Eriksson, S., Wilder, F. D., et al. 2016, JGR, 121, 11021
Sundkvist, D., Retinò, A., Vaivads, A., & Bale, S. D. 2007, PhRvL, 99, 025004
Taylor, G. I. 1938, RSPSA, 164, 476
Telloni, D., Bruno, R., & Trenchi, L. 2015, ApJ, 805, 46
TenBarge, J. M., & Howes, G. G. 2012, PhPl, 19, 055901
TenBarge, J. M., Podesta, J. J., Klein, K. G., & Howes, G. G. 2012, ApJ, 753, 107
Told, D., Jenko, F., TenBarge, J. M., Howes, G. G., & Hammett, G. W. 2015, PhRvL, 115, 025003
Treumann, R. A. 2009, A&ARv, 17, 409
Verscharen, D., Chen, C. H. K., & Wicks, R. T. 2017, ApJ, 840, 106
Verscharen, D., Marsch, E., Motschmann, U., & Müller, J. 2012, PhPl, 19, 022305
Vink, J., Broersen, S., Bykov, A., & Gabici, S. 2015, A&A, 579, A13
Vörös, Z., Yordanova, E., Echim, M. M., Consolini, G., & Narita, Y. 2016, ApJL, 819, L15
Wang, C.-P., Gkioulidou, M., Lyons, L. R., & Angelopoulos, V. 2012, JGR, 117, A08215
Yao, S., He, J.-S., Marsch, E., et al. 2011a, ApJ, 728, 146
Yao, Y., Chaston, C. C., Glassmeier, K.-H., & Angelopoulos, V. 2011b, GeoRL, 38, L09102
Yordanova, E., Vaivads, A., André, M., Buchert, S. C., & Vörös, Z. 2008, PhRvL, 100, 205003
Zocco, A., & Schekochihin, A. A. 2011, PhPl, 18, 102309